



HAL
open science

Hybrid Energy-Efficient Local Path Planning for Autonomous Vehicles in Dynamic Environments

Fadel Tarhini, Reine Talj, Moustapha Doumiati

► **To cite this version:**

Fadel Tarhini, Reine Talj, Moustapha Doumiati. Hybrid Energy-Efficient Local Path Planning for Autonomous Vehicles in Dynamic Environments. 27th IEEE International Conference on Intelligent Transportation Systems, Sep 2024, Edmonton (Canada), Canada. hal-04651719v2

HAL Id: hal-04651719

<https://hal.science/hal-04651719v2>

Submitted on 21 Nov 2024

HAL is a multi-disciplinary open access archive for the deposit and dissemination of scientific research documents, whether they are published or not. The documents may come from teaching and research institutions in France or abroad, or from public or private research centers.

L'archive ouverte pluridisciplinaire **HAL**, est destinée au dépôt et à la diffusion de documents scientifiques de niveau recherche, publiés ou non, émanant des établissements d'enseignement et de recherche français ou étrangers, des laboratoires publics ou privés.

Hybrid Energy-Efficient Local Path Planning for Autonomous Vehicles in Dynamic Environments

Fadel Tarhini¹, Reine Talj¹ and Moustapha Doumiati²

Abstract—Efficient trajectory planning plays a crucial role in the development of autonomous vehicles, ensuring safe and optimized navigation in dynamic environments. This paper proposes a novel energy-efficient hybrid trajectory planning by integrating a sampling-based method with an optimization-based path refining method. It uses the strength of the sampling-based methods to reduce the solution space and generate a reactive trajectory in a dynamic environment. Following path selection, a septic path is generated and utilized as a reference for an energy-efficient path-refining optimization problem, producing a jerk-controlled trajectory with enhanced computational efficiency. The simulations were conducted in a joint-simulation environment using Simulink/Matlab and the Scania Studio vehicle dynamics and driving environment simulator. The findings demonstrate the effectiveness of our approach in achieving significant energy savings while adeptly addressing dynamically changing environments.

I. INTRODUCTION

Advancements in automated driving mark a paradigm shift in transportation, promising enhanced safety, efficiency, and productivity. Central to this revolution is trajectory planning, a pivotal process enabling vehicles to navigate dynamic and unpredictable environments with precision and intelligence [1]. As vehicles traverse complex terrains, trajectory planning harmonizes a delicate balance, leveraging sophisticated decision-making to chart optimal paths while adhering to various constraints [2].

A trajectory planning problem entails determining the most efficient path, velocity, and orientation from the vehicle's current state to a designated goal configuration. Such optimization tasks aiming to minimize specific objectives while adhering to various constraints are recognized as PSPACE-hard problems [3]. Therefore, path-speed decoupled approaches are utilized to divide the complex problem into two distinct subproblems: spatial path planning initially, followed by speed planning [2]. This approach enables a step-by-step process, enhancing efficiency and tractability by addressing each component independently [4].

Trajectory planning methodologies are typically categorized into four main groups: learning-based, search-based, sampling-based, and optimization-based methods. Search-based methods, such as A* and state-lattice [5], [6], employ graph-based search techniques. These methods discretize the configuration space using predefined motion primitives and proactively construct a search graph for structured trajectory exploration. With appropriate heuristics and search strategies, these methods demonstrate efficacy in low-speed unstructured environments [7]. However, poorly designed search spaces can limit the solution space, resulting in suboptimal solutions or even solution unavailability despite existence. Additionally, the paths produced by graph-based methods frequently exhibit discontinuities in curvature, contributing

to elevated energy consumption and rendering them unsuitable for high-speed autonomous driving. While post-smoothing procedures can make these paths viable for on-road scenarios, they compromise the collision-free assurance initially provided by the search-based generation. Learning-based methods typically involve training a model on large datasets of sensor data and expert demonstrations to learn the mapping between input features and optimal paths [8]. For instance, [9] developed a reinforcement learning agent based on the potential field to generate a collision-free path for path tracking. While these methods have robustness to uncertainties, and the ability to incorporate complex and non-linear relationships between input features and optimal trajectories, they require extensive training data and computational resources and may struggle to generalize to unseen situations.

Sampling-based strategies can utilize random techniques like Rapidly-exploring Random Trees [10] or deterministic approaches, including control state and state space sampling methods [11], [12]. The paths generated by random sampling methods often exhibit jerky motion, redundancy, and lack of curvature continuity, making them unsuitable for autonomous driving applications at high speeds. Furthermore, the runtime of these methods is unpredictable, limiting their practical utility in real-time applications. In contrast, deterministic sampling-based methods reduce the solution space by leveraging the structure of roadways, enhancing predictability in planner behavior and reducing the selection of impractical sampling seeds. However, the optimality of the selected path is directly related to the longitudinal and lateral resolution of the generated path candidates. Improving path optimality involves reducing the resolution of generated paths, albeit increasing computational complexity. Optimization-based methods tackle two-point boundary value problems through nonlinear optimization techniques [13]. These methods excel in providing optimal solutions featuring high-order or dense waypoint curves. However, alongside computational complexity, they face challenges in managing environmental complexity which is dictated by the number of obstacles and the geometric shape of the free space.

To overcome the limitations of individual strategies, recent studies have explored integrating sampling methods with optimization techniques [14], [15], [16]. Following path selection, a refinement process is executed through nonlinear optimization aiming to minimize predefined cost functions. The authors of [15] and [16] advocate similar approaches to optimize paths selected from a set of quintic-polynomial paths by minimizing longitudinal and lateral acceleration and jerk. However, none of these approaches directly address energy efficiency concerns. Recent works in the literature target the energy efficiency objective in path planning through connected autonomous vehicles (CAVs) [17] and partially CAVs [18], or by designing energy-efficient adaptive cruise control (ACC) systems [19]. [20] proposed an energy-efficient approach for lane changing using CAVs information.

¹Université de Technologie de Compiègne, CNRS, Heudiasyc UMR 7253, CS 60 319, 60 203 Compiègne, France.

²ESEO-IREENA lab UR 4642, Nantes Université, 10 Bd Jeanneteau, 49100 Angers, France.

While existing works primarily focus on energy-efficient planning in a multi-vehicle context or through speed regulation planning, autonomous vehicles can individually reduce energy consumption through energy-optimal path generation. Therefore, this paper proposes a novel energy-efficient hybrid path planning approach by integrating sampling-based and energy optimization-based methods.

The contributions of the paper are outlined as:

- Generation of a septic reference path in the Frenet (s, q) frame to control the first, second, and third derivatives of q by s , and given to the optimization problem to enhance computational efficiency.
- Development of a novel hybrid path planning strategy by integrating sampling-based method with an energy-efficient optimization-based method.
- Validation of the planning strategy on the SCANer Studio vehicle dynamics simulator using a full non-linear vehicle model to demonstrate the effectiveness of the approach on driving comfort, energy economy, and computational efficiency.

The rest of the paper is structured as follows: Section II reveals the global system architecture. The path planning strategy is thoroughly presented in Section III. Simulation results are given in Section IV followed by the conclusion in Section V.

II. SYSTEM OVERVIEW

The global system architecture is given in Fig. 1. The perception model provides an occupancy grid representation output. Detailed discussion of this module is beyond the scope of the paper. The new footprint occupied by dynamic obstacles, within the perception zone of the vehicle, is updated at each planning iteration. The occupancy of the moving obstacles is longitudinally expanded to reflect their velocity and direction based on their predicted traveled distance. Then, the spatial path planning module, detailed in Section III, commences by a sampling-based path generation process. For each point on the navigable candidate paths, the footprint of the vehicle is validated according to the method of six circles and one large circle [3]. To improve accuracy and efficiency, the local occupancy grid is then transformed into a clearance map. The generated paths are then divided into three groups: totally navigable paths (obstacle-free paths), partially navigable paths (obstacles exist outside the security distance), and non-navigable paths (obstacles exist inside the security distance). A path selection process is then performed by choosing the best path with the minimum designed cost function. A reference septic (7th order) polynomial path is subsequently generated between the initial and final knots of the selected best path. Finally, using the septic path as an initial guess, an optimization process is conducted to minimize the discrete analog of curvature and its rate of change (jerk). Speed planning is then performed based on a cubic polynomial generation on the optimal path. Subsequently, the optimal trajectory is transferred to the control layer where the Super-Twisting Sliding Mode control is applied for path-tracking and speed control. Then, the control inputs are realized by physical actuators including four in-wheel motors. The reader can refer to the authors' previous works on this level [21], [22]. Ultimately, the steering angle and the generated torques are fed into the fully dynamic "Callas" model of the SCANer Studio professional vehicle dynamics simulator.

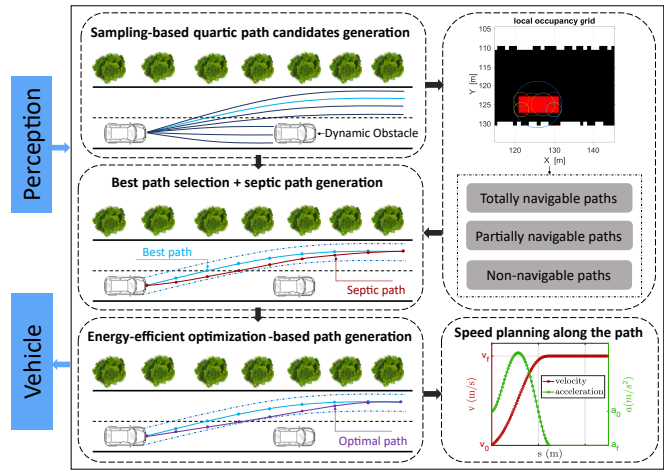


Fig. 1: Schematic diagram of the global architecture

III. PATH PLANNING

The navigation strategy unfolds in several stages, including base frame construction, generation of path candidates, obstacle detection and path classification, path selection, generation of reference septic path, and optimization to determine the optimal path.

A. Base Frame Construction

The base frame represents a global route used as a reference road information. It constitutes a sequence of waypoints and is modeled by a cubic parametric curve. Denoting s as the arc length of every segment, and i as the index of the waypoint, the cubic spline is expressed as

$$\begin{cases} x_{bf}(s) = a_0 + a_1(s - s_i) + a_2(s - s_i)^2 + a_3(s - s_i)^3 \\ y_{bf}(s) = b_0 + b_1(s - s_i) + b_2(s - s_i)^2 + b_3(s - s_i)^3 \end{cases} \quad (1)$$

where (x_{bf}, y_{bf}) are the Cartesian coordinates of the point on the base frame, and $\{(a_j, b_j), j = 0, 1, 2, 3\}$ are the fitting parameters. The heading θ_{bf} and curvature ρ_{bf} of each point on the base frame are determined by

$$\theta_{bf} = \frac{dy_{bf}}{dx_{bf}}; \quad \rho_{bf} = \frac{x'_{bf}y''_{bf} - x''_{bf}y'_{bf}}{\sqrt{(x'_{bf} + y'_{bf})^3}} \quad (2)$$

where $x'_{bf}, y'_{bf}, x''_{bf}, y''_{bf}$ are the first and second derivatives of x_{bf} and y_{bf} .

B. Path Candidates Generation

The initial step entails the localization of the vehicle within the base frame. This process involves mapping the vehicle's Cartesian coordinates to the Frenet $(s - q)$ system and subsequently determining the closest point on the base frame (denote it by $P_i(s_i, \rho_i)$) [12]. From $P_i(s_i, \rho_i)$, the path candidates are generated in a double-phase: transition phase ($s \in [s_i, s_{f0}]$) and a steady phase ($s \in [s_{f0}, s_f]$) (see Fig. 2). The length of the phases is proportional to the speed of the vehicle v and bounded between a minimum and maximum thresholds, Δs_{min} and Δs_{max} respectively (3).

$$\begin{aligned} s_{f0} &= \Delta s_{min} + k_v v \\ s_f &= \min(\Delta s_{max}, s_{f0} + 2d_{ss}) \end{aligned} \quad (3)$$

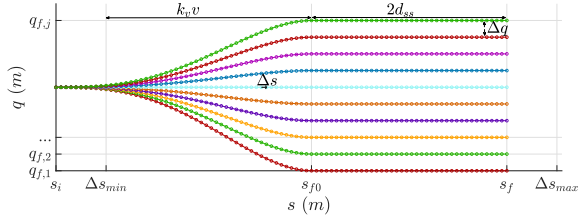


Fig. 2: Generation of the path candidates with lateral resolution Δq and longitudinal resolution Δs in the (s, q) frame.

where k_v is a gain parameter and d_{ss} is the safe stop distance, determined by

$$d_{ss} = d_{ss,0} + \frac{v^2}{2a_{dec}^{max}} \quad (4)$$

where $d_{ss,0}$ is the minimum safety gap and a_{dec}^{max} is the maximum acceptable longitudinal deceleration. To ensure the \mathcal{L}^2 continuity and avoid curvature discontinuity, the path candidates are generated based on a quartic (4th order) polynomial (5) (see Fig. 2).

$$q(s) = \begin{cases} c_0 + c_1(s - s_i) + c_2(s - s_i)^2 + c_3(s - s_i)^3 + c_4(s - s_i)^4 & s \in [s_i, s_{f0}] \\ q_{f,j} & s \in [s_{f0}, s_f] \end{cases} \quad (5)$$

The polynomial coefficients c_i of path j are determined by solving the boundary conditions problem given in (6).

$$\begin{aligned} q(s_i) &= q_i, \quad \rho(s_i) = \rho_i, \quad q(s_{f0}) = q_{f,j} \\ \frac{\partial q}{\partial s} \Big|_{s_i} &= \tan \Delta \theta_i, \quad \frac{\partial q}{\partial s} \Big|_{s_{f0}} = 0 \end{aligned} \quad (6)$$

where $\Delta \theta_i$ is the difference between the vehicle heading angle and the tangent at $P_i(s_i, \rho_i)$. Path candidates comprises a set of n points (knots) with a longitudinal resolution of distance Δs . These candidates are then mapped into the Cartesian system to conform to the maneuvering system. The corresponding points in the Cartesian system can be represented in terms of the arc length of the base frame [23] as

$$\frac{\partial x}{\partial s} = Q \cos \theta, \quad \frac{\partial y}{\partial s} = Q \sin \theta, \quad \frac{\partial \theta}{\partial s} = Q \rho \quad (7)$$

where the curvature of the path candidates, ρ , is calculated by (8).

$$\rho = \frac{S}{Q} \left(\rho_{bf} + \frac{(1 - q\rho_{bf}) \left(\frac{\partial^2 q}{\partial s^2} \right) + \rho_{bf} \left(\frac{\partial q}{\partial s} \right)^2}{Q^2} \right) \quad (8a)$$

$$Q = \sqrt{\left(\frac{\partial q}{\partial s} \right)^2 + (1 - q\rho_{bf})^2}, \quad S = \text{sgn}(1 - q\rho_{bf}) \quad (8b)$$

Upon the generation of the set of path candidates, the candidates are classified by priority, depending on the adaptive security [12], into totally navigable, partially navigable, and non-navigable paths. The selection of the best path is performed on the high-priority set of candidates. In the event that all paths within the host lane are deemed non-navigable, paths are generated in the adjacent lane, initiating overtaking if instructed by the behavioral planner. If all paths across lanes are non-navigable, emergency braking is initiated.

C. Path Selection

The path selection process is conducted to determine the best path from the set of navigable paths, minimizing

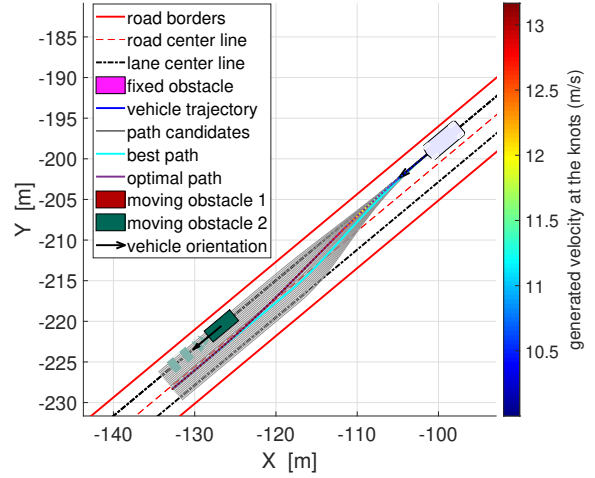


Fig. 3: Proposed trajectory planning method (common legend for Figures 5 and 7). The rectangular hatches in front of the dynamic obstacle represent its corresponding longitudinal expansion.

a cost function that incorporates various criteria (see Fig. 3). As the curve of least energy is the one with highest smoothness, J_1 is defined as an energy cost. The consistency cost J_2 can also represent an energy cost, as abrupt changes in trajectory demand additional energy and higher control effort. A reference offset cost term J_3 is also introduced to force the vehicle to maintain proximity to the reference lane. Hence, for each path i from the set of navigable paths, J_1, J_2, J_3 are given as

$$J_1[i] = \int \rho_i^2 ds \quad (9a)$$

$$J_2[i] = i^*|_t - i^*|_{t-1} \quad (9b)$$

$$J_3[i] = \int (q_i - q_{ref})^2 ds \quad (9c)$$

where q_{ref} is the lateral offset of the reference lane from the base frame and i^* is the path index. The final cost term J_4 is a safety term consisting of longitudinal safety cost $J_{4,1}$ (pertaining host lane navigability) and a lateral safety cost $J_{4,2}$ (concerning adjacent lane navigability) [12].

$$J_{4,1}[i] = 2 - \frac{2}{1 + e^{-(c_s d_{obs}[i])}} \quad (10a)$$

$$g[k] = \frac{1}{\sqrt{2\pi}\sigma} e^{-\frac{(k\Delta q)^2}{2\sigma^2}} \quad (10b)$$

$$J_{4,2}[i] = \frac{\sum_{k \in \Gamma_i} J_{4,1}[k] g[i-k]}{N} \quad (10c)$$

$$J_4[i] = J_{4,1} + w_s J_{4,2} \quad (10d)$$

where $d_{obs}[i]$ is the distance-to-obstacle (collision distance) on the path i and c_s is a tunable parameter. $g[k]$ is the discrete inverted Gaussian convolution, σ is the standard deviation of collision risk, and Δq is the lateral sampling resolution. Γ_i is the set of navigable paths excluding the path i , N is their number, and w_s is a weighting coefficient. The designed costs are normalized using (11a), and the total cost is given by (11b)

$$\bar{J}[i] = \frac{J[i] - \min(J)}{\max(J) - \min(J)} \quad (11a)$$

$$J_T[i] = w_1 \bar{J}_1[i] + w_2 \bar{J}_2[i] + w_3 \bar{J}_3[i] + w_4 \bar{J}_4[i] \quad (11b)$$

where w_1, w_2, w_3, w_4 are the weighting coefficients for energy, consistency, reference, and safety cost terms respectively. The selected path is denoted as “best path” and shown in Fig. 3.

D. Reference Septic Path

Subsequent to the best path selection, a septic path is generated between the first and final knots of the best path. The decision to use a seventh-order polynomial is based on its ability to control $\frac{\partial^3 q}{\partial s^3}$ (curvature derivative jerk), as it is the lowest order that permits imposing constraints on the jerk. The septic path in the Frenet frame is given in (12).

$$q(s) = \alpha_7 s^7 + \alpha_6 s^6 + \alpha_5 s^5 + \alpha_4 s^4 + \alpha_3 s^3 + \alpha_2 s^2 + \alpha_1 s + \alpha_0 \quad (12)$$

where $\alpha_i, i = \{0, 1, 2, \dots, 7\}$ are the polynomial coefficients. Denote by $q(s_0) = q_0, \dot{q}(s_0) = \dot{q}_0, \ddot{q}(s_0) = \ddot{q}_0, \ddot{\ddot{q}}(s_0) = \ddot{\ddot{q}}_0, q(s_f) = q_f, \dot{q}(s_f) = \dot{q}_f, \ddot{q}(s_f) = \ddot{q}_f, \ddot{\ddot{q}}(s_f) = \ddot{\ddot{q}}_f$, then α_i are calculated using the following boundary conditions.

$$q_0 = \alpha_7 s_0^7 + \alpha_6 s_0^6 + \alpha_5 s_0^5 + \alpha_4 s_0^4 + \alpha_3 s_0^3 + \alpha_2 s_0^2 + \alpha_1 s_0 + \alpha_0 \quad (13a)$$

$$\dot{q}_0 = 7\alpha_7 s_0^6 + 6\alpha_6 s_0^5 + 5\alpha_5 s_0^4 + 4\alpha_4 s_0^3 + 3\alpha_3 s_0^2 + 2\alpha_2 s_0 + \alpha_1 \quad (13b)$$

$$\ddot{q}_0 = 42\alpha_7 s_0^5 + 30\alpha_6 s_0^4 + 20\alpha_5 s_0^3 + 12\alpha_4 s_0^2 + 6\alpha_3 s_0 + 2\alpha_2 \quad (13c)$$

$$\ddot{\ddot{q}}_0 = 210\alpha_7 s_0^4 + 120\alpha_6 s_0^3 + 60\alpha_5 s_0^2 + 24\alpha_4 s_0 + 6\alpha_3 \quad (13d)$$

$$q_f = \alpha_7 s_f^7 + \alpha_6 s_f^6 + \alpha_5 s_f^5 + \alpha_4 s_f^4 + \alpha_3 s_f^3 + \alpha_2 s_f^2 + \alpha_1 s_f + \alpha_0 \quad (13e)$$

$$\dot{q}_f = 7\alpha_7 s_f^6 + 6\alpha_6 s_f^5 + 5\alpha_5 s_f^4 + 4\alpha_4 s_f^3 + 3\alpha_3 s_f^2 + 2\alpha_2 s_f + \alpha_1 \quad (13f)$$

$$\ddot{q}_f = 42\alpha_7 s_f^5 + 30\alpha_6 s_f^4 + 20\alpha_5 s_f^3 + 12\alpha_4 s_f^2 + 6\alpha_3 s_f + 2\alpha_2 \quad (13g)$$

$$\ddot{\ddot{q}}_f = 210\alpha_7 s_f^4 + 120\alpha_6 s_f^3 + 60\alpha_5 s_f^2 + 24\alpha_4 s_f + 6\alpha_3 \quad (13h)$$

where s_0 and q_0 , respectively s_f and q_f , are the coordinates of the initial and final knot of the best path in the Frenet frame. The initial conditions are determined as follows: $\dot{q}_0 = \frac{\partial q}{\partial s}|_{s_0}, \ddot{q}_0 = \frac{\partial^2 q}{\partial s^2}|_{s_0}, \ddot{\ddot{q}}_0 = \frac{\partial^3 q}{\partial s^3}|_{s_0}$, and $\dot{q}_f = \ddot{q}_f = \ddot{\ddot{q}}_f = 0$. The problem can be solved as (14).

$$\begin{bmatrix} \alpha_7 \\ \alpha_6 \\ \alpha_5 \\ \alpha_4 \\ \alpha_3 \\ \alpha_2 \\ \alpha_1 \\ \alpha_0 \end{bmatrix} = A_{[8 \times 8]}^{-1} \times \begin{bmatrix} q_0 \\ \dot{q}_0 \\ \ddot{q}_0 \\ \ddot{\ddot{q}}_0 \\ q_f \\ \dot{q}_f \\ \ddot{q}_f \\ \ddot{\ddot{q}}_f \end{bmatrix} \quad (14)$$

where A is given in (15). As the first and final knots of the septic path are the same as that of the best path, the consistency, reference, and safety costs are retained.

$$A = \begin{bmatrix} s_0^7 & s_0^6 & s_0^5 & s_0^4 & s_0^3 & s_0^2 & s_0 & 1 \\ 7s_0^6 & 6s_0^5 & 5s_0^4 & 4s_0^3 & 3s_0^2 & 2s_0 & 1 & 0 \\ 42s_0^5 & 30s_0^4 & 20s_0^3 & 12s_0^2 & 6s_0 & 2 & 0 & 0 \\ 210s_0^4 & 120s_0^3 & 60s_0^2 & 24s_0 & 6 & 0 & 0 & 0 \\ s_f^7 & s_f^6 & s_f^5 & s_f^4 & s_f^3 & s_f^2 & s_f & 1 \\ 7s_f^6 & 6s_f^5 & 5s_f^4 & 4s_f^3 & 3s_f^2 & 2s_f & 1 & 0 \\ 42s_f^5 & 30s_f^4 & 20s_f^3 & 12s_f^2 & 6s_f & 2 & 0 & 0 \\ 210s_f^4 & 120s_f^3 & 60s_f^2 & 24s_f & 6 & 0 & 0 & 0 \end{bmatrix} \quad (15)$$

Subsequently, the reference septic path serves as an initial guess for generating the optimal path.

E. Optimization-Based Path Refining

The sampling-based strategy assisted to reduce the solution space and generate a reactive path to avoid obstacles. However, the resulted best path depends on the longitudinal and lateral resolutions and hence impose limits on the motion potential of the vehicle. Specifically for lane changes, the high curvature of the best path elevates the energy consumption of the battery. To address this issue, an optimization method is proposed to minimize the image of curvature and jerk which enhances the path smoothness and consequently the energy efficiency.

The optimization problem is given in (16)

$$\min_{s_i, q_i} F_{obj} = \sum_{i=0}^{n-1} f_i(s_i, q_i) \quad (16)$$

where i is the index of the knot and n is their number. f_i is designed as follows

$$f_i = w_r \left((s_i - s_{ref})^2 + (q_i - q_{ref})^2 \right) + w_\kappa \kappa_i^2 + w_j j_i^2 \quad (17)$$

where (s_{ref}, q_{ref}) are the coordinates of the reference septic path and w_r, w_κ , and w_j are the weights on the reference, curvature, and jerk. The first term increases when the optimized path deviates from the septic reference path. κ_i and j_i are the discrete analogs of the image of curvature ($\frac{\partial^2 q_i}{\partial s_i^2}$) and jerk ($\frac{\partial^3 q_i}{\partial s_i^3}$) (curvature derivative) (18), as the paths are defined in terms of a constant longitudinal resolution Δs .

$$\kappa_i = \frac{\partial^2 q_i}{\partial s_i^2} = \frac{q_{i+2} - 2q_{i+1} + q_i}{\Delta s^2} \quad (18a)$$

$$j_i = \frac{\partial^3 q_i}{\partial s_i^3} = \frac{q_{i+3} - 3q_{i+2} + 3q_{i+1} - q_i}{\Delta s^3} \quad (18b)$$

The optimization acts to minimize the second and third rate of change of q_i at s_i , reflecting an image of lateral acceleration and its rate of change. The term κ_i permits the vehicle to run smoothly and contribute to the decrease of the resulting curvature of the optimal path. The term j_i penalizes sudden changes in the lateral acceleration and curvature. Smooth paths require less energy to traverse, as abrupt changes in acceleration and jerk lead to increased energy consumption. Therefore, both terms contribute to the overall smoothness of the optimal path, thereby enhancing energy efficiency.

The optimization problem is subjected to the kinematic constraints given in (19), and the safety constraints in (21).

$$\left| \frac{q_{i+2} - 2q_{i+1} + q_i}{\Delta s^2} \right| \leq \kappa_{max} \quad (19a)$$

$$\left| \frac{q_{i+3} - 3q_{i+2} + 3q_{i+1} - q_i}{\Delta s^3} \right| \leq j_{max} \quad (19b)$$

where κ_{max} and j_{max} are positive thresholds for the image of acceleration and jerk. Since the septic reference path is dense in waypoints and Δs is constant, the optimal path is sampled on the same s_{ref} values. Additionally, as the first and final knots of the optimal path coincide with those of the septic reference path, the initial and final conditions on $\frac{\partial q}{\partial s}, \frac{\partial^2 q}{\partial s^2}$, and $\frac{\partial^3 q}{\partial s^3}$ are preserved.

To ensure the safety of the optimal path, a set of safety and boundary constraints are imposed into the optimization problem along (19). In contrast to the six-circle decomposition method employed for collision checking in the sampling-

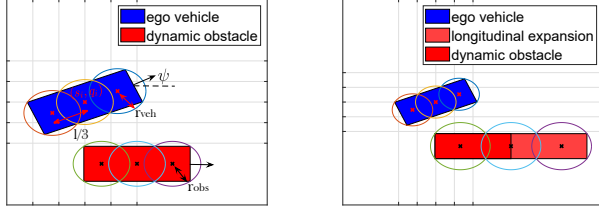


Fig. 4: Representation of the safety constraints for path optimization

based approach (refer to Fig. 1), the vehicle and obstacles are decomposed into three circles (see Fig. 4) to reduce safety constraints and improve computational efficiency. The coordinates of the centers of the circles are given in terms of the knot (s_i, q_i) of the optimal path as (20).

$$s_{1,i} = s_i; q_{1,i} = q_i \quad (20a)$$

$$s_{2,i} = s_i - (l_i/3) \cos \psi; q_{2,i} = q_i - (l_i/3) \sin \psi \quad (20b)$$

$$s_{3,i} = s_i + (l_i/3) \cos \psi; q_{3,i} = q_i + (l_i/3) \sin \psi \quad (20c)$$

where l_i is the length of the vehicle and ψ its heading angle from the reference line. The safety constraints are given by (21) where $n = \{1, 2, 3\}$ and $p = \{1, 2, 3\}$, and $(s_{n,j}, q_{n,j})$ are the center coordinates of the obstacle circles. The radius of the circles of the vehicle and that of the obstacles are r_{veh} and r_{obs} given in (22).

$$(s_{n,i} - s_{p,j})^2 + (q_{n,i} - q_{p,j})^2 \geq (r_{veh} + r_{obs})^2 \quad (21)$$

$$r_{veh} = \sqrt{\left(\frac{w_i}{2}\right)^2 + \left(\frac{l_i}{6}\right)^2}; r_{obs} = \sqrt{\left(\frac{w_j}{2}\right)^2 + \left(\frac{l_j}{6}\right)^2} \quad (22)$$

$$q_{min} \leq q_i \leq q_{max} \quad (23)$$

where l_j is the total length of the dynamic obstacle including its longitudinal expansion (see Fig. 4), and w_i, w_j are the widths of the vehicle and the obstacle. Finally, the boundary constraint (23) is enforced as a driving envelope to ensure the vehicle remains within its bounds.

The optimal path (see Fig. 3) is ultimately generated by solving (16) using the sequential quadratic programming (SQP) method [24]. With the reference septic path as the initial guess, this approach can efficiently converge to the optimal result with fewer iterations, typically approaching the vicinity of the global optimal solution.

F. Speed Planning

Speed planning is performed by generating a cubic polynomial along the optimal path. The cubic $v(t)$ is given as

$$v(t) = v_0 + \xi_1 t^1 + \xi_2 t^2 + \xi_3 t^3 \quad (24)$$

where ξ_1, ξ_2, ξ_3 are the polynomial coefficients and can be calculated by solving the following boundary conditions

$$v(t_f) = v_0 + \xi_1 t_f + \xi_2 t_f^2 + \xi_3 t_f^3 = v_f \quad (25a)$$

$$a(0) = \xi_1 = a_0 \quad (25b)$$

$$a(t_f) = \xi_1 + 2\xi_2 t_f + 3\xi_3 t_f^2 = a_f \quad (25c)$$

$$s(t_f) = v_0 t_f + \frac{1}{2} \xi_1 t_f^2 + \frac{1}{3} \xi_2 t_f^3 + \frac{1}{4} \xi_3 t_f^4 = s_f \quad (25d)$$

where v_0, a_0 and v_f, a_f are the velocity and acceleration at the initial and the final points of the polynomial. s_f represents the length of the optimal path and t_f is the traveling time along it. t_f is obtained by solving the quadratic

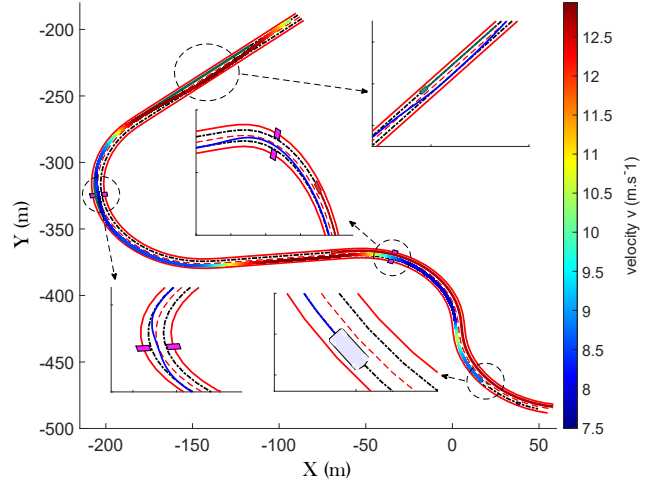


Fig. 5: Vehicle trajectory (same legend as Fig. 3)

equation (26), and $\xi_1 = a_0$ is trivial.

$$\beta_2 t_f^2 + \beta_1 t_f + \beta_0 = 0 \quad (26a)$$

$$\beta_2 = a_0 - a_f; \beta_1 = 6v_0 + 6v_f; \beta_0 = -12s_f \quad (26b)$$

Subsequently, ξ_2 and ξ_3 are given by (27). $v_0 = v(t_i)$, $a_0 = \frac{\partial v}{\partial t}|_{t_i}$, and $a_f = 0$. v_f is the desired velocity at the final knot and is given by the behavioral planner [2] (refer to the cubic polynomial generation in Fig. 1).

$$\xi_2 = \frac{(-a_f - 2a_0)t_f - 3(v_0 - v_f)}{t_f^2} \quad (27a)$$

$$\xi_3 = \frac{(a_0 + a_f)t_f + 2(v_0 - v_f)}{t_f^3} \quad (27b)$$

IV. SIMULATION RESULTS

The complete system architecture is implemented and validated in a joint simulation between Simulink/Matlab and the SCANeR Studio vehicle dynamics simulator. The planner is running at a frequency of 10 Hz, the controller is running at 50 Hz, and the rest of the system is running at 100 Hz. To illustrate the effectiveness of the proposed planning approach, the energy consumption cost E_m is examined, along with the smoothness cost of $\frac{\partial^3 q}{\partial s^3}$ which is given by

$$smoothness = \sum_{i=0}^{n-1} \left(\frac{\partial^3 q}{\partial s^3} \Big|_{i+1} - \frac{\partial^3 q}{\partial s^3} \Big|_i \right)^2 \quad (28)$$

This work considers an autonomous in-wheel driven electric vehicle, where E_m is determined as the sum of the energy consumed by the four motors in terms of motor torque, rotational velocity, and efficiency. Further, the efficiency of each motor is estimated based on the respective motor efficiency maps. For further elaboration, interested readers are directed to the authors' prior work [24].

The scenario unfolds on the track given in Fig. 5. Within this scenario, the autonomous vehicle confronts several situations: 1) overtaking a dynamic obstacle, 2) navigating a narrow passage, and 3) returning to the host lane while encountering a dynamic obstacle during in-between navigation of static obstacles at a corner. The path planning approach demonstrates effectiveness by adeptly handling the critical situations. The vehicle speed is shown to track

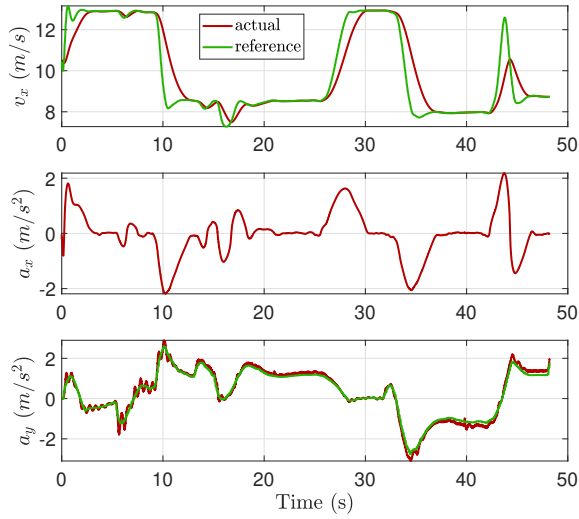


Fig. 6: Vehicle velocity v_x , longitudinal acceleration a_x and lateral acceleration a_y for the optimal strategy

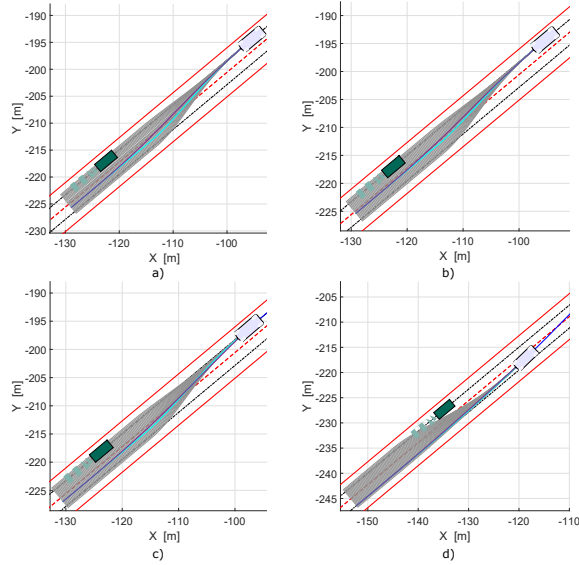


Fig. 7: Best path selection and optimal path generation in distinct timelapses (same legend as Fig. 3)

the reference generated profile in Fig. 6, along with the longitudinal and lateral acceleration (a_x and a_y respectively). Thanks to the cubic speed profiling, the vehicle speed and the longitudinal acceleration exhibited smooth profiles where a_x is maintained between -2 and 2 m/s^2 . The lateral acceleration is tracking the reference determined by ρv^2 and maintained between $[-2.5 \ 2.5] \text{ m/s}^2$ which reflects good maneuverability and comfortable driving.

The first, second, and third derivatives of q by s are given in Fig. 8. The optimal planning approach is contrasted with two other approaches. The planning strategy that follows the best path exclusively is denoted as “best path” as in [11], [12], while the strategy that follows the septic reference path is denoted as “septic reference path”. The best path selection and the optimal path generation are depicted in Fig. 7 in different time lapses. The optimal path reveals a slightly better $\frac{\partial q}{\partial s}$ and $\frac{\partial^2 q}{\partial s^2}$ than the best path, with the septic reference path oscillating at $t = 15 \text{ s}$. However, the difference is significant for $\frac{\partial^3 q}{\partial s^3}$. While the best path

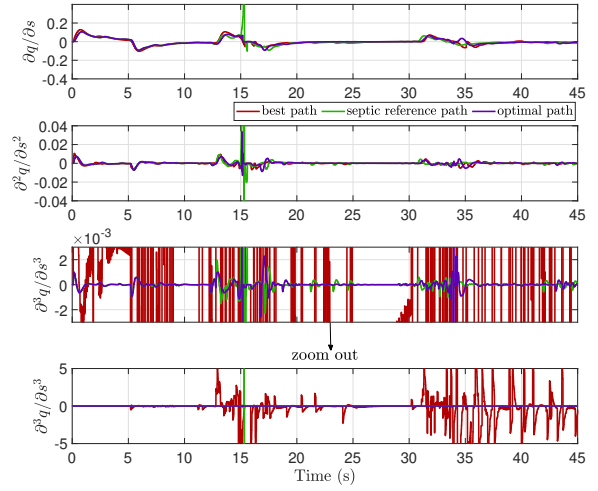


Fig. 8: First, second, and third derivatives of q by s

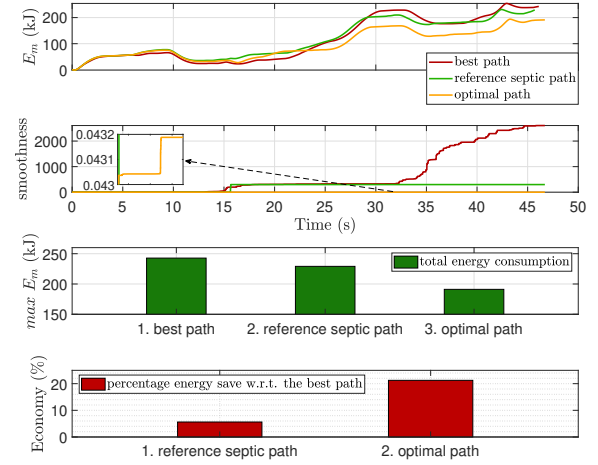


Fig. 9: Energy consumption and smoothness comparison

strategy is continually linearly oscillating (1st order $\frac{\partial^3 q}{\partial s^3}$) and reached -5 and 5 m^{-2} , the optimal path exhibited a smooth third order controlled $\frac{\partial^3 q}{\partial s^3}$ and maintained in the interval $[-3 \ 3] \times 10^{-3}$. The septic reference path revealed similar $\frac{\partial^3 q}{\partial s^3}$ with small oscillations at $t = 15 \text{ s}$. The enhanced smoothness (see Fig. 9), boundedness, and controlled jerk contribute to improved comfort and lateral stability (see Fig. 6), while also showcasing energy savings. The energy consumption, along with the smoothness cost, of the best path, reference septic path and the optimal path are given in Fig. 9. Compared to the best path, the reference septic path has achieved a 6 % energy save with a 22 % energy economy for the optimal path.

The required computational time for the optimal planning approach is given in Fig. 10. The simulations are conducted under an Intel Core i9-12950HX CPU 2.3-GHz laptop. As a result, the optimal path planning approach achieves a root mean squared of 60 ms , allowing it to operate in real-time with a sampling time of 100 ms . Further computational enhancements can be achieved by integrating more sophisticated optimization algorithms. It is worth noting that both

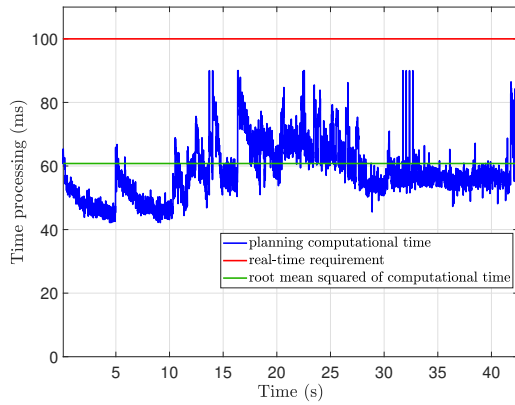


Fig. 10: Computational time of the entire process (ms)

the best path and the septic reference path planning strategies exhibit a root mean squared of 15 *ms*. Thus, the reference septic path represents a fast and energy-efficient strategy in itself.

Starting from the selected best path from the sampling-based strategy, the septic path is generated as a reference for determining the optimal path. Leveraging the discerning features of the best path profile, the septic path is generated to yield a jerk-optimal reference trajectory, serving as an initial guess for the optimization problem. This, in turn, streamlines computational efficiency as the optimal path typically lies in the vicinity of the septic path. The minimization of the image of curvature and its derivative (jerk) aims to enhance trajectory smoothness and mitigate abrupt lateral transitions, thereby fostering energy efficiency. Overall, the boundedness, smoothness, and control of the jerk in an integrated hybrid strategy demonstrate energy economy.

A video of the validation on the Scanner Studio simulator can be seen at: “<https://youtu.be/2aVhVjTgEFU>”.

V. CONCLUSION

This paper introduces a novel energy-efficient hybrid path planning approach by integrating sampling-based and optimization-based methods. Following the path selection process, a reference septic path is generated and given as an initial guess to the optimization problem. The optimal path is generated by minimizing the image of curvature and jerk, thereby enhancing path smoothness and improving energy efficiency. The proposed hybrid trajectory planning approach demonstrates effectiveness in reducing energy consumption by up to 20 % through controlled, smooth, and bounded jerk profiles, while adeptly addressing dynamic environments. Future research endeavors aim to implement and validate this planning strategy on a real experimental vehicle.

ACKNOWLEDGMENT

This work is carried out within the framework of the V3EA project “Electric, Energy Efficient, and Autonomous Vehicle” (2021-2025), funded by the Research National Agency (ANR) of the French government.

REFERENCES

- [1] V. Lefkopoulou and M. Kamgarpour, “Trajectory planning under environmental uncertainty with finite-sample safety guarantees,” *Automatica*, vol. 131, p. 109754, 2021.
- [2] F. Tarhini, R. Talj, and M. Doumiati, “Safe and energy-efficient jerk-controlled speed profiling for on-road autonomous vehicles,” *IEEE Transactions on Intelligent Vehicles*, pp. 1–16, 2024.

- [3] Y. Zhang, H. Chen, S. L. Waslander, J. Gong, G. Xiong, T. Yang, and K. Liu, “Hybrid trajectory planning for autonomous driving in highly constrained environments,” *IEEE Access*, vol. 6, pp. 32 800–32 819, 2018.
- [4] J. Cheng, Y. Chen, Q. Zhang, L. Gan, C. Liu, and M. Liu, “Real-time trajectory planning for autonomous driving with gaussian process and incremental refinement,” in *2022 International Conference on Robotics and Automation (ICRA)*, 2022, pp. 8999–9005.
- [5] Y. Guo, D. Yao, B. Li, Z. He, H. Gao, and L. Li, “Trajectory planning for an autonomous vehicle in spatially constrained environments,” *IEEE Transactions on Intelligent Transportation Systems*, vol. 23, no. 10, pp. 18 326–18 336, 2022.
- [6] K. Bergman, O. Ljungqvist, and D. Axehill, “Improved path planning by tightly combining lattice-based path planning and optimal control,” *IEEE Transactions on Intelligent Vehicles*, vol. 6, no. 1, pp. 57–66, 2021.
- [7] X. Li, Z. Sun, D. Cao, Z. He, and Q. Zhu, “Real-time trajectory planning for autonomous urban driving: Framework, algorithms, and verifications,” *IEEE/ASME Transactions on Mechatronics*, vol. 21, no. 2, pp. 740–753, 2016.
- [8] H. Lee, K. Kim, N. Kim, and S. W. Cha, “Energy efficient speed planning of electric vehicles for car-following scenario using model-based reinforcement learning,” *Applied Energy*, vol. 313, p. 118460, 2022.
- [9] Z. Qi, T. Wang, J. Chen, D. Narang, Y. Wang, and H. Yang, “Learning-based path planning and predictive control for autonomous vehicles with low-cost positioning,” *IEEE Transactions on Intelligent Vehicles*, vol. 8, no. 2, pp. 1093–1104, 2023.
- [10] R. Mashayekhi, M. Y. I. Idris, M. H. Anisi, I. Ahmady, and I. Ali, “Informed rrt*-connect: An asymptotically optimal single-query path planning method,” *IEEE Access*, vol. 8, pp. 19 842–19 852, 2020.
- [11] X. Hu, L. Chen, B. Tang, D. Cao, and H. He, “Dynamic path planning for autonomous driving on various roads with avoidance of static and moving obstacles,” *Mechanical Systems and Signal Processing*, vol. 100, pp. 482–500, 2018.
- [12] A. Said, R. Talj, C. Francis, and H. Shraim, “Local trajectory planning for autonomous vehicle with static and dynamic obstacles avoidance,” in *2021 IEEE International Intelligent Transportation Systems Conference (ITSC)*, 2021, pp. 410–416.
- [13] P. Typaldos, M. Papageorgiou, and I. Papamichail, “Optimization-based path-planning for connected and non-connected automated vehicles,” *Transportation Research Part C: Emerging Technologies*, vol. 134, p. 103487, 2022.
- [14] W. Lim, S. Lee, M. Sunwoo, and K. Jo, “Hybrid trajectory planning for autonomous driving in on-road dynamic scenarios,” *IEEE Transactions on Intelligent Transportation Systems*, vol. 22, no. 1, pp. 341–355, 2021.
- [15] M. Wang, L. Zhang, Z. Zhang, and Z. Wang, “A hybrid trajectory planning strategy for intelligent vehicles in on-road dynamic scenarios,” *IEEE Transactions on Vehicular Technology*, vol. 72, no. 3, pp. 2832–2847, 2023.
- [16] W. Lim, S. Lee, M. Sunwoo, and K. Jo, “Hierarchical trajectory planning of an autonomous car based on the integration of a sampling and an optimization method,” *IEEE Transactions on Intelligent Transportation Systems*, vol. 19, no. 2, pp. 613–626, 2018.
- [17] T. Ard, L. Guo, J. Han, Y. Jia, A. Vahidi, and D. Karbowski, “Energy-efficient driving in connected corridors via minimum principle control: Vehicle-in-the-loop experimental verification in mixed fleets,” *IEEE Transactions on Intelligent Vehicles*, vol. 8, no. 2, pp. 1279–1291, 2023.
- [18] Z. Wang, G. Wu, and M. J. Barth, “Cooperative eco-driving at signalized intersections in a partially connected and automated vehicle environment,” *IEEE Transactions on Intelligent Transportation Systems*, vol. 21, no. 5, pp. 2029–2038, 2020.
- [19] M. Shen, R. A. Dollar, T. G. Molnar, C. R. He, A. Vahidi, and G. Orosz, “Energy-efficient reactive and predictive connected cruise control,” *IEEE Transactions on Intelligent Vehicles*, vol. 9, no. 1, pp. 944–957, 2024.
- [20] E. Joa, H. Lee, E. Y. Choi, and F. Borrelli, “Energy-efficient lane changes planning and control for connected autonomous vehicles on urban roads,” in *2023 IEEE Intelligent Vehicles Symposium (IV)*, 2023, pp. 1–6.
- [21] F. Tarhini, R. Talj, and M. Doumiati, “Dynamic and real-time continuous look-ahead distance for autonomous vehicles: an explicit formulation,” *Vehicle System Dynamics*, vol. 0, no. 0, pp. 1–27, 2023.
- [22] F. Tarhini, R. Talj, and M. Doumiati, “Multi-objective control architecture for an autonomous in-wheel driven electric vehicle,” *IFAC-PapersOnLine*, vol. 56, no. 2, pp. 11 470–11 476, 2023.
- [23] T. Barfoot and C. Clark, “Motion planning for formations of mobile robots,” *Robotics and Autonomous Systems*, vol. 46, no. 2, pp. 65–78, 2004.
- [24] F. Tarhini, R. Talj, and M. Doumiati, “Dual-level control architectures for over-actuated autonomous vehicle’s stability, path-tracking, and energy economy,” *IEEE Transactions on Intelligent Vehicles*, vol. 9, no. 1, pp. 287–303, 2024.